Extracting spatial spectra using coarse-graining based on implicit filters

S. Danilov[1,2], S. Juricke[2], K. Nowak[1], D. Sidorenko[1], Q. Wang[1]

[1]Alfred Wegener Institute, Helmholtz Centre for Polar and Marine Research, Bremerhaven, Germany
[2]Constructor University, Bremen, Germany

Key Points:

- A coarse-graining technique for unstructured meshes based on implicit filters is proposed for the analysis of energy distribution over scales.
- The technique is well suited for scalar and vector quantities in both flat and spherical geometry.

Corresponding author: Sergey Danilov, sergey.danilov@awi.de

Abstract

Scale analysis based on coarse-graining has been proposed recently as an alternative to Fourier analysis. It requires interpolation to a regular mesh for data from unstructured-mesh models. We propose an alternative coarse-graining method which relies on implicit filters using powers of discrete Laplacians. This method can work on arbitrary (structured or unstructured) meshes and is applicable to the direct output of unstructured-mesh models. Illustrations and details are provided for discrete fields placed at vertices of triangular meshes. The placement on triangles is also briefly discussed.

Plain Language Summary

When studying ocean flows scientists are interested in how flow energy is distributed over scales. Ocean circulation models simulate these flows on computational meshes, and some models use highly variable meshes, such as unstructured triangular meshes. To eliminate the effect of mesh inhomogeneity, the output of such models is first interpolated to a regular quadrilateral mesh, which creates uncertainties. The method we propose does not require this interpolation and can be applied to the output of such models directly.

1 Introduction

The analysis of energy distribution over spatial scales, as well as the related analyses for energy generation, dissipation and transfer between scales are canonical tools in the study of eddy-driven flows. Typically, such analyses are conducted with the help of the Fourier transform. However, recently, an approach based on convolution, or coarsening has been proposed (Aluie et al. (2018); Sadek & Aluie (2018)). It not only provides energy distribution across scales but also gives the spatial distribution of energy at different scales. Additionally, this approach can be applied to flow domains of arbitrary shapes. Although the number of applications using this approach is still relatively limited compared to those utilizing Fourier spectra, they have demonstrated its usefulness.

Some new-generation ocean circulation models such as FESOM2 (Danilov et al. (2017)), MPAS-O (Ringler et al. (2013)) and ICON-o (Korn (2017)) are formulated on unstructured triangular meshes, or their dual, quasi-hexagonal meshes. Scale or spectral analysis of fields simulated on such meshes typically requires interpolation to regular quadrilateral grids. Similar difficulties arise even with models using regular meshes on the sphere, as these meshes are rarely uniform, except in case where a relatively small region is explored and mesh non-uniformity can be ignored.

This paper proposes an approach to scale analysis based on implicit filters. In essence, it is inspired by the work of Guedot et al. (2015), which utilizes implicit filters based on powers of the Laplacian operator is extended here to incorporate scale analysis through successive coarsening. An important aspect is that implicit filters based on Laplacians can be easily adapted to unstructured meshes in a manner similar to that described by Guedot et al. (2015) for the vertex-based data. However, some modifications are required for other data placements. It is crucial to note that discrete Laplacians may have spurious eigenvalues when data are placed at the centers of triangles or mid-edges (Klemp (2017), Danilov & Kutsenko (2019)), which will be discussed further. The concept of using implicit filters is not new. Its brief review can be found in Grooms et al. (2021) and is not repeated here. There is also a certain similarity to explicit approaches in Grooms et al. (2021) and Defferrard et al. (2020), where the idea to represent filter operators as series in powers of discrete Laplacians is exploited. In all these cases, only nearest data points are needed for computations, making it convenient for parallel applications. Although implicit filters involve using iterative solvers, the procedure is highly parallelizable and, hopefully, more stable than explicit methods on general unstructured meshes

where local mesh inhomogeneity may pose challenges. Furthermore, the discrete Laplace operators can be implemented in full spherical geometry as used in models. For vector-valued data (horizontal velocities), vector Laplacians can be used either in a vector-invariant form or with metric terms, as will be discussed in some detail in this study.

To start with, we explain the method using the one-dimensional case (Section 2). The extension necessary for horizontal fields is given in Section 3. The detail depends on the placement of discrete data and whether one deals with scalars or vectors. While our main focus is on the placement in FESOM, we also briefly discuss other placements. The analysis is applied to synthetic two dimensional fields to illustrate technical aspects. The results are also compared to those obtained with the coarsening method proposed by Aluie et al. (2018). The final sections of the paper present discussions and conclusions.

2 Elementary theory

The consideration presented here has very much in common with that in Guedot et al. (2015) and Sadek & Aluie (2018), because it incorporates elements from both approaches. Let $\phi(\mathbf{x})$ be a scalar field, with $\mathbf{x}$ lying in some domain D. We are interested in the distribution of the second moment (or variance if mean is removed) of this field over spatial scales. A coarse-graining approach, similar in spirit to that of Aluie et al. (2018) and Sadek & Aluie (2018) will be applied, but relying on implicit filters. The coarsened field $\overline{\phi}_\ell(\mathbf{x})$ will be found by solving

$$(1+\gamma(-\ell^2\Delta)^n)\overline{\phi}_\ell = \phi. \tag{1}$$

Here, Δ is the Laplacian, the smoothing scale is parameterized by ℓ, and γ is a parameter that tunes the relation of ℓ to wavenumbers, as will be explained further. The integer n defines the order of the implicit filter, which is second-order for $n = 1$ (in terminology of Guedot et al. (2015)), and order $2n$ in a general case. Equation (1) is complemented by boundary conditions on the boundary ∂D of the computational domain D, which will be discussed below.

A discrete Laplacian operator can be constructed independent of the type of the computational mesh and mesh geometry (flat or spherical), which makes the procedure suited for scale analysis on unstructured meshes.

2.1 1D case

In order to clarify some details of the method, we begin with the one-dimensional case assuming periodic boundary conditions to facilitate Fourier analysis. We assume $n = 1$ here, and explain later why larger n could be desirable.

In the Fourier space,

$$\hat{\overline{\phi}}_\ell(k) = \hat{G}_\ell(k)\hat{\phi}(k) = \frac{\hat{\phi}(k)}{1+\gamma\ell^2k^2},$$

where k is the wavenumber, the hat denotes Fourier transformed quantities and $\hat{G}_\ell(k)$ is the Fourier transform of the convolution kernel. The same notation k will be used for the absolute value of the wave vector in the discussion of energy spectra below in this section. Let E_k be the Fourier energy spectrum of the field ϕ such that the mean energy over D is obtained by summation over positive k,

$$E = \int_0^\infty E_k dk,$$

where the integral is a replacement for the sum over Fourier modes. The area-mean energy of the coarse grained field, to be denoted by $\overline{\mathcal{E}}_\ell$, will be expressed as

$$\overline{\mathcal{E}}_\ell = \int_0^\infty |\hat{G}_\ell|^2 E_k dk = \int_0^\infty \frac{E_k dk}{(1+\gamma\ell^2 k^2)^2}.$$

Clearly, $\overline{\mathcal{E}}_0 = E$. We can introduce

$$\varepsilon(\ell) = -\partial\overline{\mathcal{E}}_\ell/\partial\ell = -\int_0^\infty \frac{\partial|\hat{G}_\ell|^2}{\partial\ell} E_k dk = \frac{4\gamma}{\ell^2}\int_0^\infty \frac{k^2\ell^2 E_k \ell dk}{(1+\gamma k^2\ell^2)^3}. \tag{2}$$

The quantity $\varepsilon(\ell)$ can be considered as energy distribution over scales ℓ because

$$E = \int_0^\infty \varepsilon(\ell)d\ell, \quad \overline{\mathcal{E}}_\ell = \int_0^\infty |\hat{G}_\ell|^2 E_k dk = \int_l^\infty \varepsilon(\ell)d\ell = E - \int_0^l \varepsilon(\ell')d\ell',$$

and $\varepsilon d\ell$ can be interpreted as the energy stored between the scales ℓ and $\ell + d\ell$. This interpretation is not perfect because, in contrast to the Fourier spectrum, the contributions from different ℓ are not orthogonal, but it can still be useful in practice.

We will introduce one more derived quantity, proposed in Aluie et al. (2018) and Sadek & Aluie (2018). It can be more convenient as it presents a closer analogy to the Fourier spectrum. We define $k_\ell = 1/\ell$ and introduce

$$\overline{E}(k_\ell) = \partial\overline{\mathcal{E}}_\ell/\partial k_\ell = \int_0^\infty \frac{\partial|\hat{G}_\ell|^2}{\partial k_\ell} E_k dk = \int_0^\infty \frac{4\gamma k^2/k_\ell^2}{(1+\gamma k^2/k_\ell^2)^3} E_k \frac{dk}{k_\ell}. \tag{3}$$

The bar is used to distinguish this quantity from the Fourier energy spectrum. The form-factor $\partial|\hat{G}_\ell|^2/\partial k_\ell$ is a function of wavenumber k and has a peak at some k. It therefore picks up the energy E_k in the vicinity of that peak wavenumber and ensures that $\overline{E}(k_\ell)$ is an approximate representation of E_k. It remains to be seen what is the correspondence between the peak wavenumber k and k_ℓ, or the peak wavelength $\lambda = 2\pi/k$ and ℓ, and when $\overline{E}(k_\ell)$ represents E_k sufficiently accurately. These questions will be addressed in the following sections.

2.2 Comparison with explicit convolution kernels

A box convolution kernel with width ℓ in the k-space is

$$\hat{G}_l(k) = \frac{\sin(k\ell/2)}{(k\ell/2)}.$$

As $z = k\ell \to 0$, $\hat{G}_l(k) \approx 1 - z^2/24$. We may require that all second-order kernels have such behavior in the vicinity of zero wavenumbers. For a Gaussian filter this requirement will lead to

$$\hat{G}_l(k) = \exp(-k^2\ell^2/24).$$

For the second order implicit filter this will lead to $\gamma = 1/24$, giving

$$\hat{G}_l(k) = \frac{1}{1+k^2\ell^2/24}.$$

The left panel of Fig. 1 depicts these kernels as a function of $z = k\ell = k/k_\ell$. Note that the box kernel shows the sharpest behavior in the vicinity of zero, and the implicit second order filter is the most flat. The right panel shows the behavior of the dimensionless form-factor $k_\ell\partial|\hat{G}_\ell(k)|^2/\partial k_\ell = -z\partial_z|\hat{G}_\ell(z)|^2$. The maxima are reached at $z = \sqrt{12} \approx 3.46$ for the Gaussian and implicit second-order filter, and $z \approx 3.52$ for the box filter. Taking the approximation $k/k_\ell \approx 3.5$ we obtain $\ell = (3.5/2\pi)\lambda \approx 0.55\lambda$. As expected,

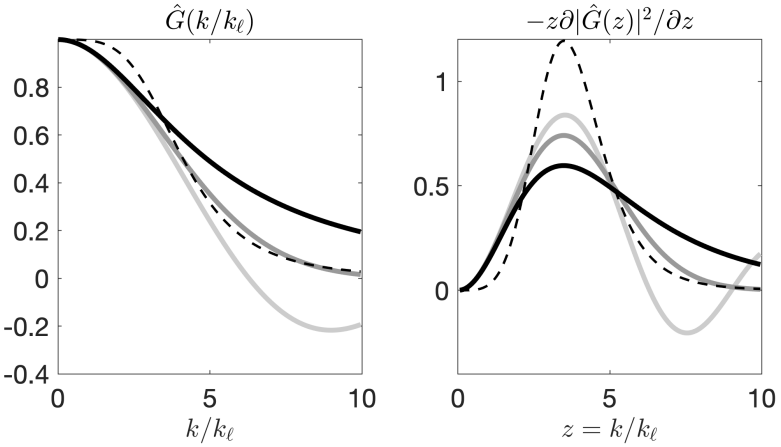

Figure 1. Convolution kernels (left) and the dimensionless form-factor $k_\ell\partial|\hat{G}_\ell(k)|^2/\partial_{k_\ell}$ (right) as functions of $z = k/k_\ell$. Shown are the box kernel (light gray), Gaussian kernel (gray), implicit second-order kernel with $\gamma = 1/24$ (black) and implicit fourth-order kernel ($n = 2$) with $\gamma = 1/288$ (dashed).

the scale ℓ is about half of a wavelength, and a more accurate statement has hardly a lot of sense since E_k is a function of k, and the peak of the integrand in (3) for given k_ℓ will occur for somewhat different k than the peak of the form-factor.

2.3 Limitations

In order to see how $\overline{E}(k_\ell)$ is related to the Fourier spectrum we assume that

$$E_k = Ck^{-\alpha}, \quad k \in (k_{\min}, k_{\max}),$$

and zero otherwise. In this case,

$$\overline{E}(k_\ell) = 4C\gamma k_\ell^{-\alpha} \int_{z_{\min}}^{z_{\max}} \frac{z^{2-\alpha}dz}{(1+\gamma z^2)^3}. \tag{4}$$

Here $z_{\min} = k_{\min}/k_\ell = k_{\min}\ell$ and $z_{\max} = k_{\max}/k_\ell = k_{\max}\ell$. The integrand in (4) does not depend on the scale ℓ, and if not for the variable integration limits, we would have concluded that $\overline{E}(k_\ell)$ has the same spectral slope as E_k just with a slightly different amplitude factor. However, the limits are functions of k_ℓ. In practical applications with discrete data, $k_{\min} = 2\pi/L_x$ and $k_{\max} = \pi/h$, where L_x and h are respectively the domain size and mesh cell size.

If $\gamma^{1/2}\ell > h/\pi$, which is generally the case, $\gamma^{1/2}z_{\max} > 1$. Since the integrand in (4) vanishes rapidly for $\gamma^{1/2}z > 1$, the precise value of the upper limit will have only a small effect. The effect of the lower limit depends on the slope α via the numerator of the integrand. If $\alpha \geq 2$, the integrand takes the largest values at the lower limit, meaning that the integral in (4) becomes sensitive to its lower limit, and that $\overline{E}(k_\ell)$ will differ from E_k for small k_ℓ. The integral will be entirely determined by the behavior at the lower limit for $\alpha > 3$. Such slopes cannot be diagnosed with second-order filters, which will return $\overline{E}(k_\ell) \sim k_\ell^{-3}$. Sadek & Aluie (2018) give an illustration of such a saturation effect for slopes steeper than -3.

Note that even if the Fourier energy spectra are sufficiently flat (e.g. with $\alpha = 5/3$), the integral in (4) can still be sensitive to the lower limit because $z^{2-\alpha}$ varies too slowly. In a more general situation, when E_k has a local spectral peak at intermediate scales,

the position of a local peak in $\overline{E}(k_\ell)$ could be aliased because the form-factor is rather broad for the second-order filters (see Fig. 1, right panel).

This is the reason why it is advisable to use higher orders n in (1). Indeed, the expression (4) for arbitrary n transforms to

$$\overline{E}(k_l) = 4n\gamma C k_\ell^{-\alpha} \int_{z_{\min}}^{z_{\max}} \frac{z^{2n-\alpha} dz}{(1+\gamma z^{2n})^3}. \tag{5}$$

For $n = 2$, i.e., for the biharmonic filter, one will need to take $\gamma = 1/288$ to have the same position of the peak in the form-factor as in the second-order case with $\gamma = 1/24$ because the peak is always at $2\gamma z^{2n} = 1$. This case is depicted in Fig. 1 with the dashed line, and the right panel illustrates that the peak becomes sharper than for the second-order filters. Importantly, the form-factor remains closer to zero at small wavenumers and is well-suited for a practically interesting range of slopes $\alpha \leq 3$. The relation between the Fourier spectrum and the scale spectrum becomes more local. Sadek & Aluie (2018) discuss the construction of high-order explicit convolution kernels and illustrate the improvements in the performance of the scale analyses with high-order kernels. We present similar illustrations for the biharmonic case later.

Note that one is free in the selection of parameter γ. For practical purposes it might be convenient to take $\gamma = 1/2$, in which case the peak is at $k = k_\ell$ and ℓ acquires the sense of inverse wavenumber.

2.4 Modifications in the discrete case

The eigenvalue of the discrete Laplacian is an approximation to $-k^2$ of the continuous case. In the one-dimensional case the simplest numerical implementation of the Laplacian operator on a regular mesh $(\mathsf{L}\phi)_j = (\phi_{j-1} + \phi_{j+1} - 2\phi_j)/h^2$, where j is the cell index and h the cell size, leads to the Fourier symbol $L_k = -(4/h^2)\sin^2(kh/2)$. For the largest resolvable wavenumber $k = \pi/h$, the ratio of discrete to continuous Fourier symbols is $-L_k/k^2 = (4/h^2)\sin^2(\pi/2)(h/\pi)^2 = 4/\pi^2$, which is not negligible.

We explore the consequences of this difference, by writing

$$\hat{G}_\ell(k) = \frac{1}{1+\gamma(-\beta L_k)^n},$$

where the scale parameter $\beta = \beta(k_\ell)$ is introduced formally instead of $\ell^2 = 1/k_\ell^2$. In this case the form-factor is

$$\partial \hat{G}_\ell^2/\partial k_\ell = \frac{-2n\gamma(-\beta L_k)^n}{(1+\gamma(-\beta L_k)^n)^3} \frac{1}{\beta} \frac{\partial \beta}{\partial k_\ell}.$$

Considering the form-factor as a function of wavenumber k, we find that it reaches maximum at

$$-2\gamma\beta L_k = 1. \tag{6}$$

We take $\gamma = 1/2$ everywhere further to simplify this condition.

There are two obvious options. We can modify the scale parameter β taking $\beta = \beta^M = -1/L_{k_\ell}$, which is similar to the correction used by Guedot et al. (2015). In this case the form-factor peaks at $k = k_\ell = 1/\ell$, so that k_ℓ acquires the sense of the standard wavenumber, which lies in the range from $2\pi/L_x$ to π/h. The drawback of this choice is that $\beta^{-1}\partial\beta/\partial k_\ell \sim \cos(k_\ell h/2)/\sin(k_\ell h/2)$, which tends to zero at $k_\ell = \pi/h$, artificially damping the scale spectrum near the cutoff wavenumber π/h.

The other choice is to leave $\beta = 1/k_\ell^2$. In this case the position of the peak of the form-factor is at $-L_k = k_\ell^2$. The relationship between k and k_ℓ depends on the eigen-

value of discrete Laplacian. For the standard 1D Laplacian we find $\sin(kh/2) = k_\ell h/2$. The peak at $k = \pi/h$ corresponds to $k_\ell = 2/h$ and the peak at $k = \pi/(2h)$ corresponds to $k_\ell = \sqrt{2}/h$. The latter values are already close, and the correspondence between the peak k and k_ℓ is recovered for smaller wavenumbers.

As is seen, both choices introduce certain complications at grid scales. However, discrete operators in ocean circulation models also contain errors at grid scales, so that the scale spectra at such scales are of limited interest. If one considers wavenumbers smaller than $\pi/(2h)$, both choices of β and respective scale spectra become close. One can also ignore the distinction between k_ℓ and the peak k in this range if $\beta = 1/k_\ell^2$, and this choice of β becomes a simpler option. We will, nevertheless, keep the option $\beta = \beta^M$ below for completeness. Guedot et al. (2015) use the 1D Laplacian eigenvalue above also on unstructured meshes, identifying h with the length of the side of a triangle, but we opt for a slightly different value, see below. Since h is variable on unstructured meshes, β^M (if used) should be included between divergence and gradient in the scalar Laplacian, and similarly in the vector Laplacian.

For the comparison with the box filter, we recall that the peak of the form-factor is at $k\ell_{\rm box} \approx 3.5$, which means that $\ell_{\rm box} \approx 3.5/k_\ell$ in terms of k_ℓ used further for implicit filters.

3 Unstructured meshes

Laplace operators on unstructured triangular meshes depend on the placement of discrete degrees of freedom. Some of them are reviewed by Klemp (2017) and Danilov & Kutsenko (2019). As applied to the existing unstructured-mesh global ocean circulation models, one needs to distinguish between the cases of vertex, cell and mid-edge placement, and the cases of scalar and vector operators. The main focus below will be on the FESOM discretization which places scalars at vertices and horizontal velocities on triangles. Although horizontal velocities in FESOM are placed on triangles, in the default implementation we seek coarse grained velocities at vertex locations because this leads to matrices with a twice smaller dimension. One may, nevertheless, need the native placement to analyze dissipation spectra, but we do not consider it in detail here, limiting ourselves only to the case of scalars placed on triangles. The particular feature of this case is that the Laplacians either contain spurious eigenvalues or a non-trivial kernel. We mention that the cell placement of scalars on hexagonal meshes in MPAS-Ocean differs from the vertex placement of FESOM only in the detail of control volumes, and that scalars are placed on triangles in ICON-o. Normal component of velocities are placed at mid-edges in MPAS-O and ICON-o. In these cases vector-invariant forms of vector Laplacians are appropriate, which will not be analysed in detail here.

The discretization of Laplacians on unstructured meshes can be obtained by finite volume (as in Guedot et al. (2015)) and finite element methods, and we briefly describe both for the vertex case. The discretization of vector Laplacian for FESOM which works with the full horizontal velocity vector (quasi B grid) can be done similarly to scalars, but with the addition of metric terms as discussed below. Using the vector invariant form of the vector Laplacian will not lead to advantages for quasi B grid.

3.1 Scalars, vertex placement

One can use either the finite volume or finite element method. They lead to slightly different discretizations on non-uniform meshes. In the first case, which is also the choice in Guedot et al. (2015),

$$A_v(\mathsf{D}\overline{\phi}_\ell)_v = \sum_{v' \in N(v)} \frac{\overline{\phi}_{v'} - \overline{\phi}_v}{l_{vv'}} \beta_{vv'} \mathbf{n}_{vv'} \cdot \mathbf{s}_{vv'}, \tag{7}$$

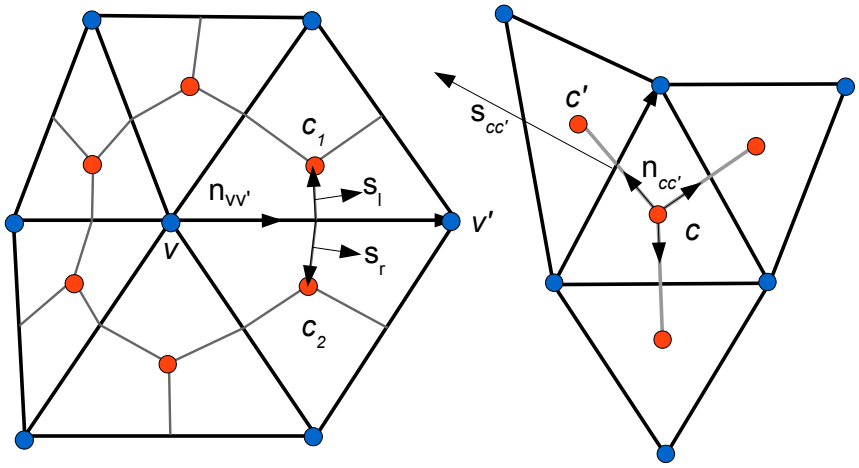

Figure 2. Finite-volume computations of Laplacians for the vertex (left) and cell (right) quantities. In the vertex case, $\mathbf{n}_{vv'}$ is the unit vector in the direction of edge, and $\mathbf{s}_{vv'} = \mathbf{s}_l + \mathbf{s}_r$, where $\mathbf{s}_l$ and $\mathbf{s}_r$ are the left and right vectors from the mid-edge to cell centers rotated to outer normal directions. In the cell case, $\mathbf{n}_{cc'}$ is the unit vector along the line connecting cell centers and $\mathbf{s}_{cc'}$ is the edge vector rotated toward the outer normal.

where the index v enumerates vertices, $N(v)$ is the set of neighboring vertices, $l_{vv'}$ is the length of the edge between vertices, $\mathbf{n}_{vv'}$ is the unit vector from v to v', $\mathbf{s}_{vv'}$ is the boundary segment vector and A_v the area of scalar median-dual control volume containing vertex v, see Fig. 2. We included the scale factor $\beta_{vv'}$ as an edge-based quantity. It can be either $\beta^M_{vv'}$ (see below) or $1/k_\ell^2$, in which case it can be taken as a factor before the sum. The quantity $\mathbf{s}_{vv'}$ is a combination of two contributions obtained by rotating vectors connecting mid-edge to cell centroids in the case of FESOM (median-dual control volume), as illustrated in Fig. 2, but it would be related to a single segment on Voronoi (hexagonal) meshes. The operator D is the discrete Laplacian (modified by the scale factor). Because of A_v on the left hand side D is not symmetric (with respect to v and v'), but the right hand side of (7) gives a symmetric operator. This is why (1) has to be discretized in area-weighted sense (see below).

Assuming $\overline{\phi}_\ell, \phi \sim e^{i\mathbf{k}\cdot\mathbf{x}}$, where $\mathbf{k} = (k, l)$ is the wave vector and $\mathbf{x}$ the coordinate vector, and further assuming that the mesh consists of equilateral triangles with the side a and height $h = a\sqrt{3}/2$, with one side oriented along the x-direction, we obtain the Fourier symbol of the vertex Laplacian (for $\beta_{vv'} = 1$)

$$L_{\mathbf{k}} = (1/h^2)[\cos(ka) + \cos(ka/2 + lh) + \cos(-ka + lh) - 3].$$

The Fourier symbol depends on the wave vector orientation. The boundary of the first Brillouin zone is closest to $\mathbf{k} = 0$ in six directions (one is $k = 0$), and in such directions $L_{\mathbf{k}} = L_K = -(4/h^2)\sin^2(Kh/2)$, where $K = |\mathbf{k}|$ (see Danilov (2022)). This expression is similar to the one discussed for the one-dimensional case, with the difference that h is not the length of the triangle side, but the triangle height. We take $\beta^M_{vv'} = -L_{k_\ell}$, where $L_{k_\ell} = L_K|_{K=k_\ell}$, and express the height assuming regular meshes, $h = \sqrt{3}l_{vv'}/2$. The wavenumber k_ℓ is the absolute value of two-dimensional wave vector and should be taken between $2\pi/L_x$ and π/h.

We will suppress the subscript ℓ in $\overline{\phi}_\ell$ further for compactness. The discrete version of equation (1) for $n = 1$ becomes

$$\mathsf{S}_{vv'}\overline{\phi}_{v'} = A_v\phi_v,$$

where summation over repeating index v' is implied. The system matrix is

$$\mathsf{S}_{vv'} = A_v\mathsf{I}_{vv'} + (1/2)A_v\mathsf{D}_{vv'}$$

with $\mathsf{I}_{vv'}$ the identity matrix and $\mathsf{D}_{vv'}$ the matrix of the operator in (7).

Taken in this form, $\mathsf{S}_{vv'}$ is a positive symmetric matrix, and solution for $\overline{\phi}$ can be obtained by the conjugate gradient method.

At this place we turn to the question of boundary conditions. The procedure of constructing the Laplacian, described above, implies that the component of gradients that are normal to domain boundaries are thought to be zero, i.e. we are dealing with the case of zero von Neumann boundary conditions. One can also use the Dirichlet boundary conditions requiring that $\overline{\phi} = \phi$ at boundary points, but it will introduce small scales at the boundary. If these conditions are selected, the simplest way to implement them consists in leaving only the diagonal entries due to $A_v\mathsf{I}_{vv'}$ in row v of $\mathsf{S}_{vv'}$ if v is at the boundary. Note that the symmetry of $\mathsf{S}_{vv'}$ will be destroyed. One more choice is to extend the mesh into land and set ϕ to zero there, which might reduce the sensitivity to boundary conditions. We use von Neumann boundary conditions in all cases below, but the question of optimal boundary conditions requires further attention.

In the case of a biharmonic filter the matrix of the biharmonic operator can be obtained by applying the procedure used for D twice,

$$\mathsf{S}_{vv''} = A_v\mathsf{I}_{vv''} + (1/2)A_v\mathsf{D}_{vv'}\mathsf{D}_{v'v''},$$

with summation over v' implied. Although $\mathsf{D}_{v'v''}$ includes division over $A_{v'}$, the combination $A_v\mathsf{D}_{vv'}\mathsf{D}_{v'v''}$ is symmetric.

Equation (1) can also be discretized with the help of the finite element method. Although it leads to a similar expression for scalars, it is our preferred approach because it is also more useful for vector Laplacians as concerns the metric terms. Consider first the case $n = 1$. We obtain the weak formulation of (1) by multiplying it with some sufficiently smooth function $w(\mathbf{x})$, integrating over the domain D and transforming the Laplacian term by integration by parts,

$$\int_D (w\overline{\phi} + (1/2)\beta\nabla w\cdot\nabla\overline{\phi})dS = \int_D w\phi dS.$$

Here the boundary term appearing after the integration by parts is set to zero, which corresponds to natural boundary conditions, similarly to the finite-volume derivation. We write the discrete fields as series $\overline{\phi} = \sum_{v'}\overline{\phi}_{v'}N_{v'}(\mathbf{x})$ and $\phi = \sum_{v'}\phi_{v'}N_{v'}(\mathbf{x})$, where $N_v(\mathbf{x})$ is a piecewise linear basis function. This function equals 1 at $\mathbf{x}_v$, decays to 0 at vertices connected to v by edges, and is zero outside the stencil of nearest triangles. To obtain continuous Galerkin approximation we require that the weak equation above is valid if w is any of the N_v,

$$(\mathsf{M}_{vv'} + (1/2)\mathsf{D}_{vv'})\overline{\phi}_{v'} = \mathsf{M}_{vv'}\phi_{v'},$$

where $\mathsf{M}_{vv'} = \int N_vN_{v'}dS$ is the mass matrix and $\mathsf{D}_{vv'} = \int\beta\nabla N_v\cdot\nabla N_{v'}dS$. The diagonally lumped approximation of mass matrix is $M^L_{vv'} = A_v\mathsf{I}_{vv'}$. If this approximation is applied, we get the same final discretization on uniform equilateral meshes as for the finite volume method except for the treatment of β. Since computation of integrals are done on triangles (mesh cells), the scaling parameter is treated as a cell quantity if

the modified option is used. Gradients of linear basis functions are constant on triangles, and their integration is just multiplication with triangle area. The height of triangle in $L_{k\ell}$ on cell c is conveniently expressed in terms of triangle area as $h = 3^{1/4}\sqrt{A_c}$ if the modified scaling parameter is used. Once again, we have symmetric matrices. The implementation of biharmonic operator leads to $\mathsf{D}(\mathsf{M}^L)^{-1}\mathsf{D}$. An alternative approximate implementation is to eliminate weighting with triangular areas in D, add the factor $1/2$ in D to compensate for the difference between triangle area and the area associated to a vertex, and replace M with the identity matrix I. It is used in our examples below as it implies slightly less work.

3.2 Spherical geometry and vertex-based vector Laplacians

FESOM uses longitude-latitude coordinates in spherical geometry (for detail, see Danilov et al. (2017)). The cosine of latitude is approximated by a constant on triangles and local distances on each triangle are calculated in a local Cartesian frame, with x and y aligned with local zonal and meridional directions. The areas of triangles are computed assuming that triangles are flat, and areas of scalar control volumes are obtained by taking $1/3$ of the area of all triangles joining at a given vertex. This way of treating spherical geometry is fully compatible with the finite element computations described in the previous section. For the finite volume treatment, the length of edges is determined using the cosine at mid-edges.

Although horizontal (zonal and meridional) velocities in FESOM are placed at triangles, in the present implementation the filtered velocities are calculated at vertices because there are twice fewer vertices than triangles, and matrices to be iteratively inverted have twice lower dimension.

Let $\overline{\mathbf{u}} = (\overline{u}, \overline{v})$ be the filtered horizontal velocity, and $\mathbf{u} = (u, v)$ the original velocity (we suppress the ℓ subscript here too). We will use index v for vertex-based velocities, and index c for cell-based original velocities. The weak equation will take the form

$$\int_D (\mathbf{w}\cdot\overline{\mathbf{u}} + (1/2)\beta\nabla\mathbf{w} : \nabla\overline{\mathbf{u}})dS = \int_D \mathbf{w}\cdot\mathbf{u}dS,$$

where now $\mathbf{w}$ is the vector-valued smooth function. Writing $\overline{\mathbf{u}} = \sum_{v'} \overline{\mathbf{u}}_{v'} N_{v'}(\mathbf{x})$, $\mathbf{u} = \sum_c \mathbf{u}_c M_c(\mathbf{x})$, where M_c is the indicator function equal 1 on triangle c and 0 outside it, and requiring that the weak equation is valid for $\mathbf{w} = \mathbf{w}_v N_v$ for any vertex v, we obtain the set of discrete equations. However, because the unit zonal and meridional vectors are varying, there will be additional metric terms in the expression for velocity gradient,

$$\nabla\mathbf{u} = \begin{pmatrix} \partial_x u - mv & \partial_x v + mu \\ \partial_y u & \partial_y v \end{pmatrix},$$

and similarly in the expression for the gradient of test function $\mathbf{w}$. Here, $m = \tan\theta/R_e$, with θ the latitude and R_e earth's radius. Combining all metric terms, we will get the following x and y equations

$$(\mathsf{M}_{vv'} + (1/2)\mathsf{D}_{vv'})\overline{u}_{v'} + \mathsf{T}_{vv'}\overline{v}_{v'} = \mathsf{R}_{vc}u_c, \tag{8}$$

$$(\mathsf{M}_{vv'} + (1/2)\mathsf{D}_{vv'})\overline{v}_{v'} - \mathsf{T}_{vv'}\overline{u}_{v'} = \mathsf{R}_{vc}v_c, \tag{9}$$

where $\mathsf{T}_{vv'} = \int(-\partial_x N_v + \partial_x N_{v'})\beta m dS$ is the operator accounting for metric terms and $\mathsf{R}_{vc} = \int N_v M_c dS$ is the right hand side operator which is the projection operator onto the space of piecewise linear functions. Summation is implied over repeating indices in matrix-vector products.

The metric terms couple equations for $\overline{u}$ and $\overline{v}$, and the dimension of system matrix becomes twice larger than for scalar fields. While it can still be solved, the metric terms can be accounted approximately if wavelengths $2\pi/k_\ell$ are not very large by putting

them on the right hand side and estimating them from the solution for the nearest available k_ℓ. For the largest k_ℓ they can be estimated using the original field. On basin scales, this approximation is not necessarily sufficient and the full system has to be solved.

3.3 Scalars, cell placement

The smallest-stencil Laplacian in this case is obtained using the finite volume method and is written similarly to (7)

$$A_c(\mathsf{D}\overline{\phi})_c = \sum_{c' \in N(c)} \frac{\overline{\phi}_{c'} - \overline{\phi}_c}{l_{cc'}} \beta_{cc'} \mathbf{n}_{cc'} \cdot \mathbf{s}_{cc'}. \tag{10}$$

Here summation is over the neighbors of cell (triangle) c, which are the cells that have common edges with c (see Fig. 2), $l_{cc'}$ is the distance between the cell centers, A_c is the cell area, $\mathbf{n}_{cc'}$ is the unit vector in the direction from c to c' and $\mathbf{s}_{cc'}$ is the cell side vector rotated to the direction of the outer normal. For meshes used in discretizations of C-grid type, the c points are associated with circumcenters. In this case the vectors $\mathbf{n}_{cc'}$ and $\mathbf{s}_{cc'}$ have the same direction, and this expression presents the divergence of gradient. If c is associated with cell centroids, on distorted meshes one accounts only for the component of gradient in the direction of $\mathbf{n}_{cc'}$ while full gradient is formally needed (discretization (7) has similar limitations). More precise computations are of course possible, but they will not be considered here. Although such details introduce some uncertainty in the analysis, they will basically affect only grid scales.

To estimate the eigenvalues of this Laplacian, we use a uniform equilateral mesh, setting $\beta_{cc'} = 1$ in (10). In order to find the eigenvalues we first note that for any two neighboring triangles the orientation of stencils of neighbors depends on the orientation of triangles themselves. For this reason, an elementary Fourier harmonic is described by two amplitudes and the Fourier symbol becomes a 2 by 2 matrix (see e.g. Klemp (2017), Danilov & Kutsenko (2019)), with two eigenvalues

$$L_{\mathbf{k}} = (4/a^2)(-3 \pm |V|), \quad V = e^{-2ilh/3} + e^{ika/2+ilh/3} + e^{-ika/2+ilh/3}.$$

The plus sign corresponds to the physical eigenvalue which tends to $-k^2-l^2$ in the limit of small wavenumbers. The minus sign corresponds to a numerical eigenvalue which is anomalously high in absolute value (it tends to $-24/a^2$ in the limit of small wavenumbers).

In the direction $k = 0$, $|V|^2 = 5 + 4\cos(Kh)$, which corresponds to a more accurate behavior than in the vertex case above, giving the physical $L_{\mathbf{k}}$ equal to $-6/h^2$ instead of $-\pi^2/h^2$ at the largest wavenumber. The eigenvector of the numerical eigenvalue corresponds to a grid-scale pattern that may potentially be present because of a slight difference in differential operators on differently oriented triangles. However, even if data contain some contributions that project on the numerical mode, these contributions will be strongly damped in the filtered fields if the implicit filter is used. In contrast, the presence of spurious eigenvalues could be problematic for explicit filters based on series in Laplacians.

An alternative approach is to use a discrete Laplacian that is based on a wider stencil. An obvious choice is to reconstruct full gradient vectors on triangles based on the values on three neighboring triangles. Gradients are then averaged to edges, and their divergence gives a Laplacian (see, e.g. Danilov & Kutsenko (2019)). It turns out that such a discrete Laplacian has the same physical eigenvalue as the vertex Laplacian above, i.e. it is less accurate. Its numerical eigenvalue is zero. This Laplacian would be less useful for implicit filter applications because it will preserve grid-scale noise in coarse-grained fields. A combination of this Laplacian with the smallest-stencil Laplacian can be a way to reduce spurious eigenvalue for applications with explicit filters.

3.4 Other discretizations

The scalar Laplacian (10) can be applied to the components of cell horizontal velocity in plane geometry. Metric terms need to be added in spherical geometry, we do not discuss them here. The vector-invariant form of the vector Laplacian,

$$\Delta\mathbf{u} = \nabla\nabla\cdot\mathbf{u} - \mathrm{curl}\,\mathrm{curl}\mathbf{u}$$

would allow one to avoid the question on metric terms. It depends on computations of the divergence and inner curl. For cell velocities a natural way would be to compute the divergence and curl at vertex control volumes using the divergence and circulation theorems because velocities are known at boundaries of such control volumes. This would lead to an analog of the wider-stencil Laplacian discussed in the previous section, which is not necessarily optimal because of its large kernel.

C-grid types of discretizations used in MPAS-O and ICON-o will rely on the vector-invariant forms of vector Laplacians. These Laplacians have large spurious eigenvalues (see e.g. Klemp (2017) and Danilov & Kutsenko (2019)), but for the reasons mentioned above, this is rather an advantage.

3.5 Comments on solving procedure

As recommended by Guedot et al. (2015), instead of solving

$$\mathsf{S}\overline{\boldsymbol{\phi}} = \boldsymbol{\phi},$$

where $\overline{\boldsymbol{\phi}}$ and $\boldsymbol{\phi}$ are the vectors of discrete values, one works with perturbations $\boldsymbol{\phi}' = \overline{\boldsymbol{\phi}} - \boldsymbol{\phi}$, with the result

$$\mathsf{S}\boldsymbol{\phi}' = \boldsymbol{\phi} - \mathsf{S}\boldsymbol{\phi}.$$

In this case the right hand side has emphasis on small scales, and $\boldsymbol{\phi}'$ is the fine-scale contribution that has to be removed from the original data. This is expected to improve the convergence, which is more difficult for large scales. It indeed leads to some improvements in our case, however the main issue is that conditioning of S worsens as k_ℓ decreases.

Also, as explained by Guedot et al. (2015), one will split the operators when $n > 2$. For example,

$$\mathsf{I} + \gamma(\mathsf{D})^3 = (\mathsf{I} + \gamma^{1/3}\mathsf{D})(\mathsf{I} - \gamma^{1/3}\mathsf{D} + \gamma^{2/3}\mathsf{D}^2),$$

and

$$\mathsf{I} + \gamma(\mathsf{D})^4 = (\mathsf{I} + (4\gamma)^{1/4}\mathsf{D} + \gamma^{1/2}\mathsf{D}^2)(\mathsf{I} - (4\gamma)^{1/4}\mathsf{D} + \gamma^{1/2}\mathsf{D}^2),$$

and so on ($\gamma = 1/2$). In principle, using tri-harmonic and bi-biharmonic operators only doubles the work of iterative solvers once matrices of harmonic and biharmonic operators D and D^2 are available. While biharmonic operator should be sufficient in most cases for general conclusion about energy spectra, one may opt for higher-order in the case when precise position of spectral peaks has to be estimated.

4 Illustrations

For illustrations here we first generate a scalar field $\phi(\mathbf{x})$ on a regular quadrilateral mesh covering a square domain with size $L_x = 1024$ km. The initial mesh has the resolution $a = 4$ km (the side of quadrilateral cell). The field ϕ is initially specified at vertices of this mesh by taking random values uniformly distributed around zero. It is Fourier transformed, and each wave component is divided by $K^{(\alpha+1)/2}$, where K is the absolute value of the wave vector. After that, the inverse Fourier transform is carried out. In this way, fields with Fourier power spectra $E_K \sim K^{-\alpha}$ are created, and $\alpha =$

2 is used below. The Fourier amplitudes are additionally modified to add peaks in Fourier power spectra in section 4.2.

One triangular mesh is obtained by bisecting the quadrilateral cells of the primary mesh. The other one is an equilateral mesh with triangle side a. The third mesh is an unstructured mesh with the triangle sides varying between a and $2a$. These meshes will be denoted further as Q, E and U. One more unstructured mesh with resolution similar to U, but covering a circular area, will be used for tests in spherical geometry. The largest resolvable wavenumber is defined by the small side of triangles on mesh Q, the height of triangle on mesh E and the height of largest triangles on mesh U. The initial field on mesh Q is the constructed one, and it is linearly interpolated to meshes E and U, respectively. Except for Fig. 3, we use the modified β. We take $\gamma = 1/2$ which ensures that k_ℓ corresponds to the ordinary wavenumber and ℓ has the sense of inverse wavenumber. A conjugate gradient solver is used in all cases. In all figures showing spectral density, the vertical axis is in units of the field squared times km/cycle, and wavenumbers on the horizontal axis are in cycle/km.

4.1 Uniform and distorted triangular meshes

Two panels of Fig. 3 present the computed scale spectra on triangular meshes Q, E, and U using harmonic (right) and bi-harmonic (left) filter for realizations of field ϕ with the power density slope $\alpha = 2$. Here, the scaling factor $\beta = 1/k_\ell^2$. The Fourier spectrum is in red, it contains fluctuations because it is the spectrum of a realization. Different realizations are used in the left and right panels. The thin dashed line corresponds to the slope of -2, and blue, solid black and green lines give scale spectra on meshes Q, E, and U respectively. The horizontal axis correspond to K for the Fourier spectrum and k_ℓ for the scale spectra. The k_ℓ values are sampled up to π/h, where h is the smaller side of triangle on mesh Q or the height of the smallest triangle on other two meshes. Since $\beta = 1/k_\ell^2$, in this case we should stop at $2/h$, comparing the value of scale spectrum at this k_ℓ to the value of Fourier spectrum at $K = \pi/h$.

As expected, for the original data (blue curves) the bi-harmonic filter ensures a closer agreement between the scale and Fourier spectra. As already mentioned, the biharmonic filter can also be used for sufficiently steep spectra (formally $\alpha \le 5$), while the use of harmonic filter is limited to $\alpha \le 3$. We checked this, but do not demonstrate it here.

The scale spectra on meshes E and U (solid black and green curves) deviate from the scale spectrum on mesh Q for large k_ℓ. This is the consequence of using interpolated data on these meshes which have smaller variance on grid scales (note that E and Q curves are very close). The effect is stronger for U mesh because it contains larger triangles and for the biharmonic case (left panel) because of the narrower form-factor. For the harmonic filter, the effect is partly masked by excessively broad form-factor which picks up the contributions from smaller wavenumbers.

The scale spectra tend to bend down compared to the Fourier spectrum on the side of smallest wavenumbers, which is presumably because a part of form-factor curve is cut on the left. Similar tendency on the side of large wavenumbers is partly related to the difference between K and k_ℓ in this case.

Apart from effects caused by interpolation, the scale spectra are insensitive to the mesh type, which proves that the method can work on different meshes, including unstructured meshes. The scale spectra are always smoother than the realization of the Fourier spectrum, as they correspond to the integration over some range of Fourier wavenumbers in the vicinity of k_ℓ, which smooths the fluctuations of the Fourier spectrum. On a practical side this means that one may need less averaging over field realizations as compared to the Fourier spectrum.

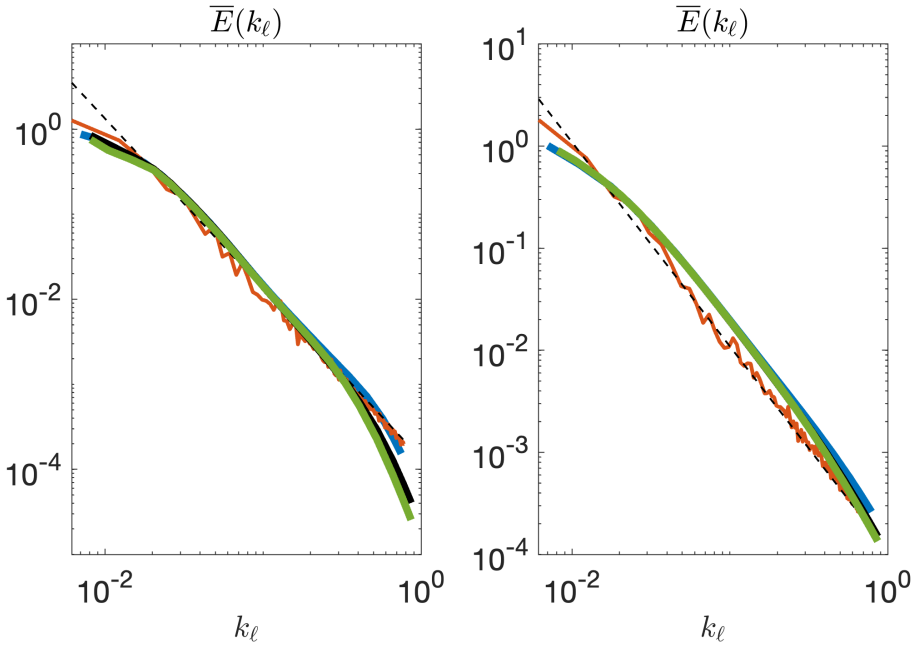

Figure 3. Scale spectra compared to Fourier spectra computed with Laplacian smoothing (right) and biharmonic smoothing (left). Shown are the Fourier spectrum (red), the scale spectrum on a uniform triangular mesh obtained by bisecting quadrilateral cells (blue, mesh Q), on a regular equilateral mesh (solid black, mesh E) and on an irregular unstructured mesh (green, mesh U). The wavenumber is in cycle/km, the horizontal axis corresponds to K for the Fourier spectrum and to $k_\ell = 1/\ell$ for scale spectra.

For unstructured meshes, the largest resolved wavenumber is formally set by the the height of the *largest* triangles. However, if such triangles cover only a small part of domain, the contribution from small triangles will still dominate. This is why we use the same largest k_ℓ for E and U meshes in practice. It is expected that the computed scale spectrum will bend down if k_ℓ is taken beyond the range, indicating where one has to stop.

4.2 Peak detection

All further examples use the modified β, so that the correspondence between the wavenumbers K and k_ℓ is maintained. Fields with peaks in the Fourier spectrum have been constructed following the same procedure as above, but applying additional factors to the amplitudes of Fourier harmonics. Figure 4 displays two examples illustrating possible behavior. We use mesh Q and the biharmonic filter. In the left panel, the peak in the Fourier spectrum is accurately recovered in the scale spectrum. In contrast, the close peaks in the scale spectrum in the right panel are not detected, and the peak around $k_\ell \approx 0.2$ cycle/km is nearly missed. The success in the first case is because the Fourier spectrum decays sufficiently fast on both sides of the peak and there are no other close peaks. The form-factor responsible for the correspondence between the Fourier and scale spectra is still not sharp enough for the field used in the right panel, even for the biharmonic filter, and higher-order filters have to be used if finding exact position of peaks is of utmost importance.

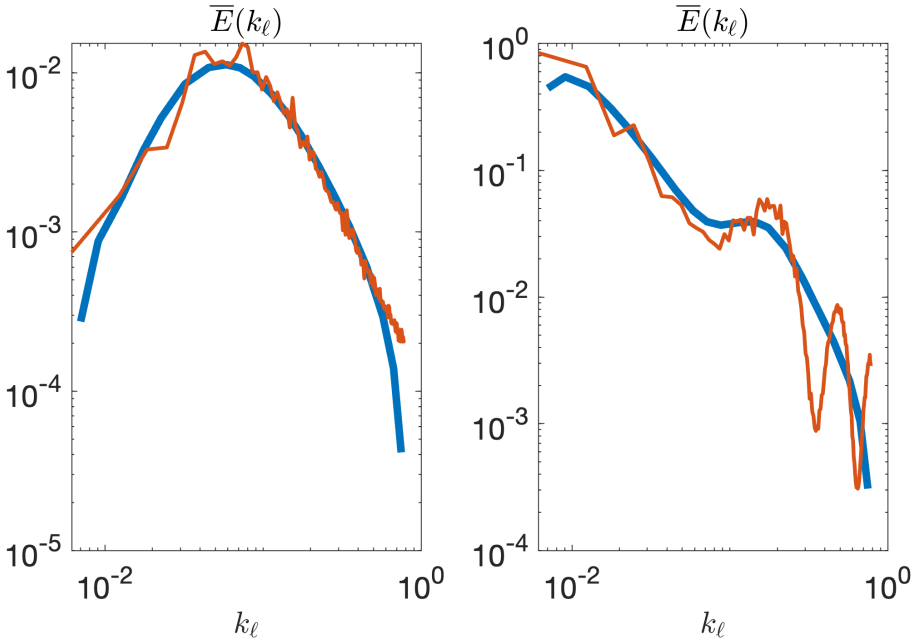

Figure 4. Spectral peak detection by scale spectra based on biharmonic smoothing. The Fourier spectra are in red, the scale spectra are in blue. Peaks can be missed or masked if they are narrow and/or there are neighboring intervals with high spectral density.

4.3 Harmonic filter vs explicit box-type filter

We use a box-type filter with the kernel

$$G(\mathbf{x}) = A(1 - \tanh(c(|\mathbf{x}| - 1.75/k_\ell)/a)), \tag{11}$$

where A is the normalization constant selected so as to ensure that $\int G(\mathbf{x})d\mathbf{x} = 1$, a is the (fixed) mesh cell size, $c = 1.3$ is a numerical factor controlling the sharpness of the box filter transition, and $1.75/k_\ell$ is equivalent to the scale $\ell_{\rm box}/2$ of the box filter, as discussed above. Figure 5 compares the scale spectrum obtained by explicit coarse-graining with this box-type filter (blue line), with the scale spectrum obtained by Laplacian smoothing (solid black line) on mesh Q. Both methods lead to nearly the same spectra, with the largest differences on the side of large wavenumbers. The selection of parameter c was experimental. Decreasing it increases the discrepancy between the two curves, which is still smaller than the deviation from the Fourier spectrum. If c is increased, the box filter transition becomes sharper, but this leads to some unevenness of the spectrum on the side of largest wavenumbers. We conclude that both methods agree, as expected, and that the attribution $\ell_{\rm box} = 3.5/k_\ell$ works well. The excessive decay at the spectral end ($k_\ell \geq 0.5$ cycle/km) shown by solid black line is the consequence of using the modified β in the analysis.

4.4 Spherical geometry

An unstructured variable-resolution mesh covering a circular area with diameter 1024 km is created. The sides of triangles vary between $a = 4$ km and $2a$. The realization of $\phi(\mathbf{x})$ with -2 power spectrum is linearly interpolated on this mesh. The mesh coordinates are then approximately transformed to longitude and latitude by multiplying the coordinates with $180/(\pi R_e)$. The sphere is then rotated in the meridional direction by $\pi/6$, $\pi/3$ and $5\pi/12$ to produce three variants of the same mesh having various

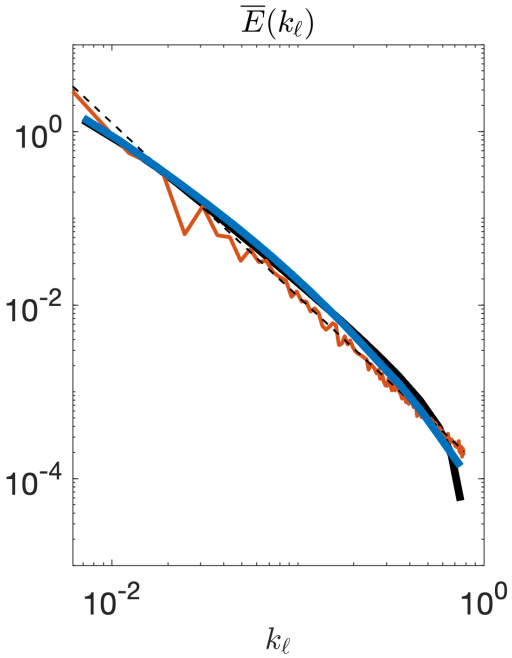

Figure 5. Scale spectra obtained by explicit coarse-graining with box filter (11) (blue) compared to scale spectra computed with Laplacian smoothing (solid black). The Fourier spectrum is in red, and the dashed line corresponds to the slope of -2.

longitude and latitude coordinates, as shown in Fig. 6. We apply the coarse-graining based on the biharmonic filter to these three meshes. Although they correspond to the same original mesh and data, they have different coordinates on the sphere and the cosine of latitude varies much stronger on the higher-latitude mesh than on the other two meshes. However, the computed scale spectra, shown in Fig. 7, are indistinguishable. This indicates that the approximation of cosine by a constant value on triangles is sufficient. By using a circular mesh in this example we illustrate that the smoothing procedure can work in a domain of arbitrary shape.

4.5 Kinetic energy spectra in spherical geometry

For this test case, a realization of scalar field $\phi(\mathbf{x})$ with power spectrum with a -4 slope was created on mesh Q. This field was interpreted as a streamfunction and used to compute a velocity field. The mesh coordinates were transformed to longitude and latitude by multiplying them by $180/(\pi R_e)$. Then the mesh was moved along the zeroth meridian so that its south-west corner is at $(0°, 75°)$. The mesh becomes stretched zonally if viewed in longitude-latitude coordinates on the sphere. Velocities are computed at the centers of triangles by computing derivatives of streamfunction given at vertices. We solved the full system of equations (8,9), building matrices with twice the dimension of the scalar problem. Figure 8 shows the scale spectrum for kinetic energy computed with the harmonic filter (blue curve). For comparison, the black curve shows the spectrum computed by solving two problems for velocity components with metric terms ignored. As is seen, the differences start to form at the large scale, and they might be larger if the size of the domain is larger. In the example used, solving (8,9) takes nearly the same computational time as solving two smaller-size problems for velocity components separately, but requires more storage.

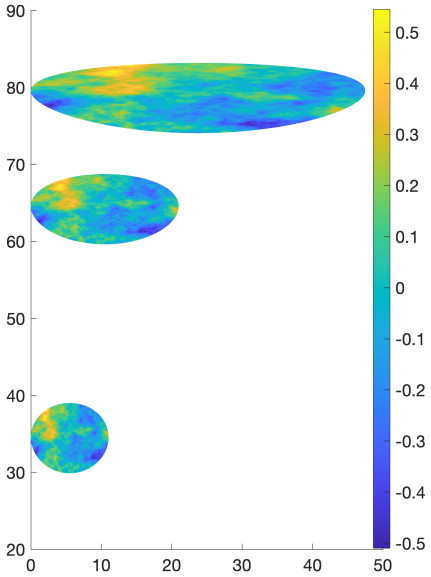

Figure 6. Three variants of the same realization of ϕ and mesh in longitude-latitude coordinates (axes in degrees).

5 Discussions

In this work we present an elementary theory of scale analysis based on implicit filters that use powers of Laplacian. Since discrete Laplacian can be written for any mesh type, the procedure is sufficiently general. Our focus was on triangular meshes, but the definition such as (7) are valid for arbitrary meshes

Discrete Laplacians deviate from their continuous counterparts on grid scales and may have spurious modes in a general case. We used only the simplest optionsfor discrete Laplacians and explored in some detail the case of vertex placement. The deviation of eigenvalues of discrete Laplacians from the continuous case creates some difficulties in the interpretation of scale spectra near the spectral end. Using the modified scale factor similar to Guedot et al. (2015) allows one to keep the correspondence between $k_\ell = 1/\ell$ and the standard wavenumber, but creates an artificial spectral decay, as seen in Figs. 5, 7 and 8. If the original definition $\beta = 1/k_\ell^2 = \ell^2$ is retained, the direct correspondence between K and k_ℓ is violated near the spectral end. While these difficulties are not important in many practical cases, one may be interested in studying energy pileup at grid scales, where the method based on implicit smoothing should be used with care.

More accurate discrete Laplacians will reduce these difficulties. The construction of such Laplacians for general unstructured meshes is, however, not straightforward, and remapping between K and k_ℓ can be an easier way if $\beta = 1/k_\ell^2$ is used. In fact, one does not necessarily need the exact correspondence between the Fourier and scale spectra, in practice it would be sufficient just to compare spectra in terms of k_ℓ. Note that similar complications may accompany the use of box-type filters if $\ell_{\text{box}}/2$ becomes close to the width of transition part (see (11)).

Although our examples include only energy spectra, the procedure is applicable for cross-spectra of two fields. Our main focus was on scale spectra $\overline{E}(k_\ell)$,which are similar to the Fourier spectra, but the scale spectrum $\epsilon(\ell)$ also deserves attention and might be similarly informative in practice.

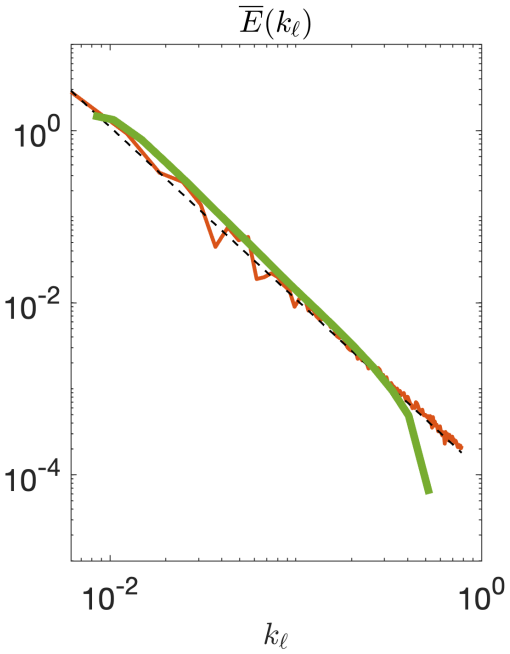

Figure 7. Scale spectra computed for three meshes in Fig. 6 using the biharmonic filter. The spectrum for the high-latitude variant is in green, and two other cases are under it. The red line corresponds to the Fourier spectrum on the parent regular quadrilateral mesh, and the dashed line gives the slope -2.

The convergence of conjugate gradient solver slows down as k_ℓ is approaching $k_{\min}$, and this slowdown becomes stronger when mesh resolution is increased. The biharmonic filter requires many more solver iterations than the harmonic one in this case and the solver should also be run with smaller tolerance in this case. The convergence can be improved through the use of preconditioners. Guedot et al. (2015) used diagonal preconditioning, but it does not provide a substantial improvement for small k_ℓ in our case. In test implementation (in Matlab), the incomplete Cholesky preconditioner was efficient on regular meshes for the harmonic filter in essentially reducing the number of iterations (but not the execution time), however there are difficulties with using it on unstructured meshes or with the biharmonic filter. It remains to be seen which preconditioners and solution methods will be able to improve the performance for general meshes.

Meshes with 1M wet vertices (the size of a typical quarter degree global mesh) can be treated in a serial way, requiring about 5 min for the construction of scale spectrum. A parallel implementation is needed for larger meshes. Both online and offline versions can be of interest. The online computations are straightforward for harmonic filters because they can rely on the existing solvers for the implicit sea surface height in FESOM and some other models. For biharmonic filters, the implementation in matrix form will require increasing halos to include neighbors of neighbors. A matrix-free form does not require the increased halos, but might complicate the design of preconditioners. Respective development is a subject of ongoing work.

We did not try the higher-order filters (tri-harmonic, bi-biharmonic or higher) in this work. They might be needed to compute spectra that contain peaks. Technically, once discrete harmonic and biharmonic operators are available, any higher-order implicit filters can be realized as a sequence of more elementary inversions that use harmonic and biharmonic operators. Practical implementation, convergence issues and the selection of the filter order need additional studies.

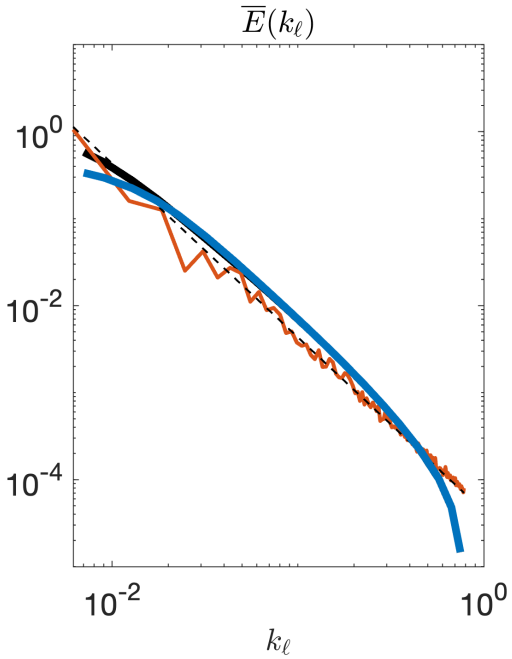

Figure 8. Scale spectra of kinetic energy computed using the biharmonic filter. The mesh is approximately between 75 and 85 degrees of latitude. The spectrum calculated taking into consideration all metric terms is represented in blue, while the spectrum without considering the metric terms is shown in black. The red line corresponds to the Fourier power spectrum of streamfunction multiplied with K^2, and the dashed line indicates the slope -2.

We experimented only with vertex placements for coarse-grained quantities, mostly because we intended to minimize the work in this study which explores and explains the concept. The cell (triangle) and edge placement will be addressed in future. In particular, for FESOM, which places horizontal velocities on triangles, the analysis of kinetic energy dissipation calls for computation on the original locations. Indeed, the projection of horizontal viscosity term from triangles to vertices may eliminate a significant part of small-scale dissipation, and computations on native locations will be made available in the future. The placement of coarse-grained velocities on triangles will lead to matrices with a twice larger dimension compared to the vertex case and a substantial increase in the required numerical work.

Finally, as mentioned before, one of the advantages of the coarse-graining approach lies in the availability of spatial distributions of energy (or other quantities). These distributions allow one to learn not only which scales contain most of the energy, but also where this energy is mainly located. This aspect was not addressed in this work, which relies on synthetic data, but it can present even larger interest than spectra in practical cases.

6 Conclusions

We propose to use implicit filters to extend the concept of scale analysis based on coarse-graining to general unstructured meshes. The procedure is based on the discretizations of Laplacian operators and can provide filters of high-order if higher degrees of Laplacian are used. The discretization can be applied to scalar and vector data, both in flat and spherical geometry.

We demonstrated the effectiveness of the implicit coarse-graining approach through several examples, highlighting the similarity between scale spectra and standard Fourier spectra, as well as its ability to operate on diverse mesh types.

We acknowledge that numerous details regarding the extension of this approach to alternative data placements still need to be tested, which is the subject of ongoing research.

7 Data availability statement

Matlab scripts used for computations in this work and data used to draw the figures can be found in Danilov et al. (2023). An accelerated Python version is under development and will be presented separately.

Acknowledgments
This work is a contribution to projects M3 and S2 of the Collaborative Research Centre TRR181 "Energy Transfer in Atmosphere and Ocean" funded by the Deutsche Forschungsgemeinschaft (DFG, German Research Foundation) - Projektnummer 274762653.

References

Aluie, H., Hecht, M., & Vallis, G. K. (2018). Mapping the energy cascade in the North Atlantic Ocean: The coarse-graining approach. *Journal of Physical Oceanography*, *48(2)*, 225–244. doi: https://doi.org/10.1175/jpo-d-17-0100.1

Danilov, S. (2022). On the resolution of triangular meshes. *Journal of Advances in Modeling Earth Systems*, *14*, e2022MS003177. doi: https://doi.org/10.1029/2022MS003177

Danilov, S., Juricke, S., Nowak, K., Sidorenko, D., & Wang, Q. (2023). Computing spatial spectra using implicit filters.
doi: https://doi.org/10.5281/zenodo.8171835

Danilov, S., & Kutsenko, A. (2019). On the geometric origin of spurious waves in finite-volume discretizations of shallow water equations on triangular meshes. *J. Comput. Phys.*, *398*, 108891.

Danilov, S., Sidorenko, D., Wang, Q., & Jung, T. (2017). The Finite-volumE Sea ice–Ocean Model (FESOM2). *Geosci. Model Dev.*, *10*, 765–789.

Defferrard, M., Milani, M., Gusset, F., & Perraudin, N. (2020). DeepSphere: A graph-based spherical CNN. *ICLR 2020*. doi: https://arXiv.org/2012.15000v1

Grooms, I., Loose, N., Abernathey, R., Steinberg, J. M., Bachman, S. D., Marques, G., ... Yankovsky, E. (2021). Diffusion-based smoothers for spatial filtering of gridded geophysical data. *Journal of Advances in Modeling Earth Systems*, *13*, e2021MS002552. doi: https://doi.org/10.1029/2021MS002552

Guedot, L., Lartigue, G., & Moureau, V. (2015). Design of implicit high-order filters on unstructured grids for the identification of large-scale features in large-eddy simulation and application to a swirl burner. *Physics of Fluids*, *27(4)*, 045107. doi: https://doi.org/10.1063/1.4917280

Klemp, J. (2017). Damping characteristics of horizontal Laplacian diffusion filters. *Mon. Weather Rev.*, *145*, 4365–4379.

Korn, P. (2017). Formulation of an unstructured grid model for global ocean dynamics. *J. Comput. Phys.*, *339*, 525–552.

Ringler, T., Petersen, M., Higdon, R., Jacobsen, D., Maltrud, M., & Jones, P. (2013). A multi-resolution approach to global ocean modelling. *Ocean Modell.*, *69*, 211–232.

Sadek, M., & Aluie, H. (2018). Extracting the spectrum of a flow by spatial filtering. *Physical Review Fluids*, *3(12)*, 124610. doi: https://doi.org/10.1103/physrevfluids

.3.124610